Hindawi Publishing Corporation
EURASIP Journal on Advances in Signal Processing
Volume 2010, Article ID 398385, 10 pages
doi:10.1155/2010/398385

Research Article

Contourlet Filter Design Based on Chebyshev Best Uniform Approximation

Guoan Yang,[1] Xiaofeng Fang,[2] Mingli Jing,[1] Songjun Zhang,[2] and Ming Hou[1]

[1] *School of Electronics and Informations, Xi'an Jiaotong University, Xi'an 710049, China*
[2] *School of Science, Xi'an Jiaotong University, Xi'an 710049, China*

Correspondence should be addressed to Guoan Yang, gayang@mail.xjtu.edu.cn

Received 11 June 2009; Revised 2 January 2010; Accepted 17 March 2010

Academic Editor: Yasar Becerikli

The contourlet transform can deal effectively with images which have directional information such as contour and texture. In contrast to wavelets for which there exists many good filters, the contourlet filter design for image processing applications is still an ongoing work. Therefore, this paper presents an approach for designing the contourlet filter based on the Chebyshev best uniform approximation for achieving an efficient image denoising applications using hidden Markov tree models in the contourlet domain. Here, we design both the optimal 9/7 wavelet filter banks with rational coefficients and new pkva 12 filter. In this paper, the Laplacian pyramid followed by the direction filter banks decomposition in the contourlet transform using the two filter banks above and the image denoising applications in the contourlet hidden Markov tree model are implemented, respectively. The experimental results show that the denoising performance of the test image Zelda in terms of peak signal-to-noise ratio is improved by 0.33 dB than using CDF 9/7 filter banks with irrational coefficients on the JPEG2000 standard and standard pkva 12 filter, and visual effects are as good as compared with the research results of Duncan D.-Y. Po and Minh N. Do.

1. Introduction

Images have been effectively modeled using the wavelet transform [1–4], which offers a mutliscale and time-frequency localized image representation. But the major drawback of wavelets in two-dimensions is its limited ability in capturing directional information [5, 6]. To overcome this deficiency, recently, many researchers have considered both the mutliscale and mutlidirectional representations that can capture the intrinsic geometrical structures such as smooth contours in natural images. The examples include the steerable pyramid, brushlets, complex wavelets, and the curvelet transform [5–8]. In particular, the curvelet transform, pioneered by Candès and Donoho, is shown to be optimal in a certain sense for functions in the continuous domain with curved singularities. In addition, Do and Vetterli developed the contourlet transform based on an efficient two-dimensional mutliscale and mutlidirectional filter banks that can deal effectively with images having smooth contours [9–11]. The contourlets not only possess the main features of wavelets but also offer a high degree of directionality and anisotropy. We know that the contourlet transform consists of the Laplacian pyramid (LP) and direction filter bank (DFB), and the core issue is a filter design problem [12–14]. The main advantage of the contourlets is that they allows for different and flexible number of directions compare with other mutliscale directional transform such as ridgelet and curverlet, achieving nearly critical sampling [15, 16]. Moreover, the basis functions of contourlet transform can be oriented at any power of 2's number of directions with flexible aspect ratios. Since the contourlet transform possesses a rich set of basis functions, it can represent a smooth contour with fewer coefficients compared with wavelets. Here, the contourlet transform is implemented via a two-dimensional filter bank for decomposing an image into several directional subbands at multiple scales. Therefore, the corresponding location and direction in image contours using the contourlet transform can produce significant coefficients.

However, in contrast to wavelets for which there exist many good wavelet filters [17–21], at present a few types of the LP and the DFB can be used for the contourlets,

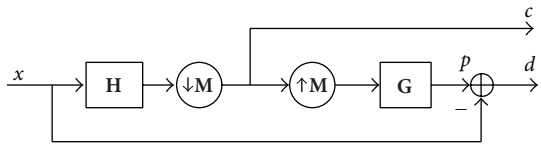

Figure 1: The LP decomposition of contourlets.

so the filter design problem for the contourlets is still an ongoing work. Therefore, the only existing wavelets filter banks are utilized directly such as the 9/7, 5/3 and Haar wavelet filter banks, and pkva filter [22, 23]. To solve this problem, we proposed here new approach for designing the contourlet filter banks based on the Chebyshev best uniform approximation for image denoising applications in the contourlet transform domain.

The paper is organized as follows. In Section 2, we give the basic structure and its inherent relationship between the LP and the DFB in the contourlets. In Section 3, we propose a design approach for contourlet filter based on the Chebyshev best uniform approximation, and give all the parameters of new contourlet filter banks using the Parks-McClellan algorithm, and new 9/7 filter banks based on author's previous works are also presented. In Section 4, we illustrate an HMT models and their resolutions for an image denoising in the contourlet domain. In Section 5, we give the experimental results and their discussion. Finally, Section 6 is about the conclusions and future works of this paper.

2. Structure of Contourlet Transform

2.1. Laplacian Pyramid. The LP decomposition has derived a coarse approximation of the original signal adopting both the lowpass filtering and downsampling. Based on this coarse approximation, we can predict the original signal and also can calculate the difference as the prediction error [11], are shown in Figure 1.

Here, the column vectors of original signals are written as $x = [x(n) : n \in \mathbb{Z}^d]^T$; then we can express these operations as the following matrix multiplication:

$$\mathbf{c} = \mathbf{H}\mathbf{x}, \qquad \mathbf{p} = \mathbf{G}\mathbf{c}. \tag{1}$$

In general, $\mathbf{H}$ has $\{\widetilde{h}(n - \mathbf{M}k)\}_{n\in\mathbb{Z}^d}$ as its rows and $\mathbf{G}$ has $\{g(n - \mathbf{M}k)\}_{n\in\mathbb{Z}^d}$ as its columns. The difference signal of the LP can be written as

$$\mathbf{d} = \mathbf{x} - \mathbf{p} = \mathbf{x} - \mathbf{G}\mathbf{H}\mathbf{x} = (\mathbf{I} - \mathbf{G}\mathbf{H})\mathbf{x}. \tag{2}$$

By combining the previous relations, we can express the analysis operator of the LP as follows:

$$\underbrace{\begin{bmatrix}\mathbf{c}\\ \mathbf{d}\end{bmatrix}}_{\mathbf{y}} = \underbrace{\begin{bmatrix}\mathbf{H}\\ \mathbf{I} - \mathbf{G}\mathbf{H}\end{bmatrix}}_{\mathbf{A}}\mathbf{x}. \tag{3}$$

The usual inverse transform of the LP is as follows:

$$\widehat{\mathbf{x}} = \underbrace{\begin{bmatrix}\mathbf{G} & \mathbf{I}\end{bmatrix}}_{\mathbf{S}_1}\begin{bmatrix}\mathbf{c}\\ \mathbf{d}\end{bmatrix}. \tag{4}$$

It is easy to verify that $\mathbf{S}_1\mathbf{A} = \mathbf{I}$ for any $\mathbf{H}$ and $\mathbf{G}$, which the LP can be perfectly reconstructed (PR) with any pair of filters $\mathbf{H}$ and $\mathbf{G}$. Since the LP is an over-complete representation, it must be treated as a frame operator [24]. A key consideration is that one should use the dual frame operator for the PR. The LP frame offers a simple scheme that has lower computational complexity, which can also be easily extended to higher dimensions space, with small redundancy. Moreover, the frame operator for the LP is expressed by a left matrix multiplication with $\mathbf{A}$. Since the LP is an over-complete representation, its frame operator allow for an infinite number of left inverses. Among those, the most important is the dual frame operator or the pseudo inverse of $\mathbf{A}$ as follows:

$$\mathbf{A}^{\dagger} = \left(\mathbf{A}^T\mathbf{A}\right)^{-1}\mathbf{A}^T. \tag{5}$$

In the polyphase representation, the pseudoinverse of $\mathbf{A}(z)$ is given by

$$\mathbf{A}^{\dagger}(z) = (\mathbf{A}^*(z)\mathbf{A}(z))^{-1}\mathbf{A}^*(z). \tag{6}$$

Thus, the basic structure of the LP modeling is described completely.

A drawback of the LP is implicit oversampling [25]; thus the LP is usually replaced by subband decomposition or wavelet transform which are a critically sampled for an image compression or denoising applications and so on. In particular, the resulting bandpass signals of the LP do not suffer from the aliasing frequencies as in the critical sampling applications. Therefore, we can generate a set of directional subband images at multiple scales satisfied the critical sampling.

2.2. Directional Filter Banks. We know that the filter banks play an important role in terms of both the theoretical and practical sense for the image processing applications. In general, the basis function of filter banks is implemented in the one-dimensional case. For the higher dimensions, the classical approach is to extend one-dimension transform to higher dimensions using the separable filter banks. Thus, both theory and practice can be completed under the low complexity implementation.

However, we know that the nonseparable filter banks and corresponding basis function can also be constructed in $\mathbf{M}$ dimensions case [26]. In addition, the quincunx filter banks (QFBs) which are most representative for image processing in the contourlet domain serves as the core of the DFB. Here, the sampling operations are defined on lattices. The lattices in d dimensions are represented by a $d \times d$ nonsingular integer matrix $\mathbf{M}$ as

$$\mathrm{LAT}(\mathbf{M}) = \left\{\mathbf{m} : \mathbf{m} = \mathbf{M}\mathbf{n},\ \mathbf{n} \in \mathbb{Z}^d\right\}. \tag{7}$$

In other words, the indices of points belonging to the sublattice LAT($\mathbf{M}$) are described as weighted integer combinations of the columns of $\mathbf{M}$. The original lattices are assumed to be $\mathbf{Z^d}$. So that the following matrices are a possible representations of the two-dimensional quincunx sublattices in which one out of two points is retained as follows:

$$\mathbf{Q}_0 = \begin{bmatrix} 1 & -1 \\ 1 & 1 \end{bmatrix}, \qquad \mathbf{Q}_1 = \begin{bmatrix} 1 & 1 \\ -1 & 1 \end{bmatrix}. \tag{8}$$

For an $\mathbf{M}$-fold downsampling the input $\mathbf{x}(\mathbf{n})$ and the output $\mathbf{x}_d(\mathbf{n})$ are as follows:

$$\begin{aligned} \mathbf{x}_d(\mathbf{n}) &= \mathbf{x}(\mathbf{Mn}), \\ \mathbf{X}_d(\boldsymbol{\omega}) &= \frac{\mathbf{1}}{|\det(\mathbf{M})|} \sum_{\mathbf{k}\in\mathbb{N}(\mathbf{M}^T)} \mathbf{X}\left(\mathbf{M}^{-T}\boldsymbol{\omega} - 2\pi\mathbf{M}^{-T}\mathbf{k}\right). \end{aligned} \tag{9}$$

Note that here $\mathbb{N}(\mathbf{M})$ is defined as the set of integer vectors of the form $\mathbf{M}t$, where $t \in [0,1)^d$. The number of elements in $\mathbb{N}(\mathbf{M})$ equals that of $|\det(\mathbf{M})|$. The matrix $\mathbf{M}^{-T} = (\mathbf{M}^T)^{-1}$ generates the reciprocal lattices of LAT($\mathbf{M}$), which consists of points representing the replicated spectra in the frequency domain. For an $\mathbf{M}$-fold upsampling, the input $\mathbf{x}(\mathbf{n})$ and the output $\mathbf{x}_u(\mathbf{n})$ are written by

$$\begin{aligned} \mathbf{x}_u(\mathbf{n}) &= \begin{cases} \mathbf{x}(\mathbf{M}^{-1}\mathbf{n}), & \text{if } \mathbf{n} \in \mathrm{LAT}(\mathbf{M}), \\ 0, & \text{otherwise}, \end{cases} \\ \mathbf{X}_u(\boldsymbol{\omega}) &= \mathbf{X}\left(\mathbf{M}^T\boldsymbol{\omega}\right), \\ \mathbf{X}_u(z) &= \mathbf{X}(z^{\mathbf{M}}). \end{aligned} \tag{10}$$

There are special cases when the sampling operations use unimodular integer matrices. Sampling using a unimodular integer matrix does not change the data rate but only rearranges the input samples, so that it is turned into a resampling operation. The following four basic unimodular matrices are utilized in the DFB in order to provide the equivalence with the rotation operations:

$$\begin{aligned} \mathbf{R}_0 &= \begin{bmatrix} 1 & 1 \\ 0 & 1 \end{bmatrix}, \qquad \mathbf{R}_1 = \begin{bmatrix} 1 & -1 \\ 0 & 1 \end{bmatrix}, \\ \mathbf{R}_2 &= \begin{bmatrix} 1 & 0 \\ 1 & 1 \end{bmatrix}, \qquad \mathbf{R}_3 = \begin{bmatrix} 1 & 0 \\ -1 & 1 \end{bmatrix}. \end{aligned} \tag{11}$$

Note that here $\mathbf{R}_0\mathbf{R}_1 = \mathbf{R}_2\mathbf{R}_3 = \mathbf{I}_{2\times 2}$. A commonly used method in analyzing mutlidimensional multirate operations is the Smith form that can diagonalize any integer matrix $\mathbf{M}$ into a product UDV, where $\mathbf{U}$ and $\mathbf{V}$ denotes the unimodular integer matrices, and $\mathbf{D}$ denotes an integer diagonal matrices, respectively. And then the quincunx matrix $\mathbf{Q}_0$ and $\mathbf{Q}_1$ can also be expressed a Smith form as follows:

$$\begin{aligned} \mathbf{Q}_0 &= \mathbf{R}_1\mathbf{D}_0\mathbf{R}_2 = \mathbf{R}_2\mathbf{D}_1\mathbf{R}_1, \\ \mathbf{Q}_1 &= \mathbf{R}_0\mathbf{D}_0\mathbf{R}_3 = \mathbf{R}_3\mathbf{D}_1\mathbf{R}_0, \end{aligned} \tag{12}$$

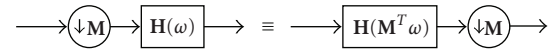

Figure 2: Identity for the analysis filter bank.

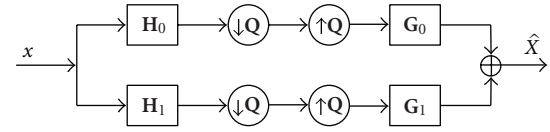

Figure 3: Quincunx filter banks.

where

$$\mathbf{D}_0 = \begin{bmatrix} 2 & 0 \\ 0 & 1 \end{bmatrix}, \qquad \mathbf{D}_1 = \begin{bmatrix} 1 & 0 \\ 0 & 2 \end{bmatrix} \tag{13}$$

are two diagonal matrices that correspond to dyadic sampling in each dimension. For the interchange of filtering and sampling, multirate identities can be used. The identity for the analysis filter $\mathbf{H}(\boldsymbol{\omega})$ is shown in Figure 2. Downsampling using $\mathbf{M}$ followed by filtering with a filter $\mathbf{H}(\boldsymbol{\omega})$ is equivalent to filtering with the filter $\mathbf{H}(\mathbf{M}^T\boldsymbol{\omega})$, which is obtained by upsampling $\mathbf{H}(\boldsymbol{\omega})$ by $\mathbf{M}$, before downsampling.

The synthesis filter $\mathbf{G}(\boldsymbol{\omega})$ can also be derived similarly. In addition, let us analyze the QFB shown in Figure 3; here we only consider the quincunx sampling matrix $\mathbf{Q}$ to be either $\mathbf{Q}_0$ or $\mathbf{Q}_1$.

And then, using (9) and (10), the input-output relationship of the QFB can be written as

$$\begin{aligned} \hat{\mathbf{X}}(\boldsymbol{\omega}) &= \frac{1}{2}[\mathbf{H}_0(\boldsymbol{\omega})\mathbf{G}_0(\boldsymbol{\omega}) + \mathbf{H}_1(\boldsymbol{\omega})\mathbf{G}_1(\boldsymbol{\omega})]\mathbf{X}(\boldsymbol{\omega}) \\ &\quad + \frac{1}{2}[\mathbf{H}_0(\boldsymbol{\omega}+\boldsymbol{\pi})\mathbf{G}_0(\boldsymbol{\omega}) + \mathbf{H}_1(\boldsymbol{\omega}+\boldsymbol{\pi})\mathbf{G}_1(\boldsymbol{\omega})]\mathbf{X}(\boldsymbol{\omega}+\boldsymbol{\pi}), \end{aligned} \tag{14}$$

where $\boldsymbol{\pi} = [\pi \quad \pi]^T$. Note that there is similarity between this expression and the one for the two channels filter bank in one-dimension. Thus, results in the one-dimension counterpart can be extended to the quincunx scheme. In particular, the QFB provides a biorthogonal expansion while it satisfies the following PR condition:

$$\begin{aligned} \mathbf{H}_0(\boldsymbol{\omega})\mathbf{G}_0(\boldsymbol{\omega}) + \mathbf{H}_1(\boldsymbol{\omega})\mathbf{G}_1(\boldsymbol{\omega}) &= 2, \\ \mathbf{H}_0(\boldsymbol{\omega}+\boldsymbol{\pi})\mathbf{G}_0(\boldsymbol{\omega}) + \mathbf{H}_1(\boldsymbol{\omega}+\boldsymbol{\pi})\mathbf{G}_1(\boldsymbol{\omega}) &= 0. \end{aligned} \tag{15}$$

Here, the PR conditions imply that the synthesis filters are expressed through the analysis filters as follows:

$$\mathbf{G}_0(z) = z^{\mathbf{k}}\mathbf{H}_1(-z), \qquad \mathbf{G}_1(z) = -z^{\mathbf{k}}\mathbf{H}_0(-z). \tag{16}$$

The QFB can be used to split the frequency spectrum of the input signal into a lowpass and a highpass channels using a diamond-shaped filter pair, or into a horizontal and a vertical channel using a fan filter pair. Frequency characteristics of these filters are shown in Figure 4, where the regions 0 denote the diamond and fan filter, respectively; the regions 1 denote the otherwise.

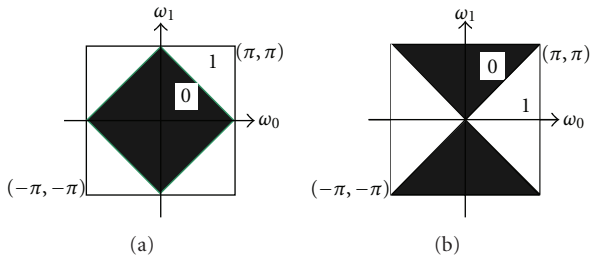

Figure 4: Diamond and fan filter of (a) and (b).

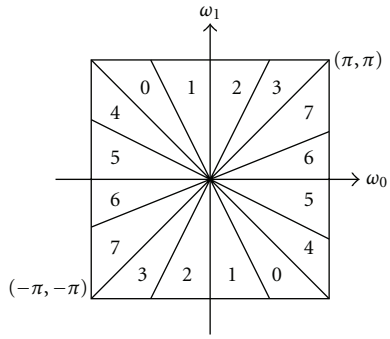

Figure 5: Directional filter bank frequency partitioning $\ell = 3$ and there are $2^3 = 8$ real wedge-shaped frequency bands.

Therefore, we can obtain one filter pair from the other through simply modulating the filters using π in either the ω_0 or ω_1 frequency variable. From (15) it can be found that if the same modulation is applied to both analysis and synthesis filters then the PR conditions are satisfied. Thus, the design issue for the fan QFB turn into a design of diamond-shaped QFB. Moreover, the DFB is implemented efficiently via a ℓ-level tree-structured decomposition that leads to 2^ℓ subbands with wedge-shaped frequency partition as shown in Figure 5.

To all the sampling matrix on the channel k ($0 \le k < 2^{\ell-1}$) in a ℓ-levels DFB, $\ell \ge 2$, we have

$$\mathbf{M}_k^{(\ell)} = 2 \cdot \mathbf{D}_0^{\ell-2}\mathbf{R}_3^{s_\ell(k)}, \tag{17}$$

where $s_\ell(k) = 2\lfloor k/2 \rfloor - 2^{\ell-2} + 1$, and the expressions for the sampling matrices in (17) are as follows:

$$\mathbf{R}_3^{-s_\ell(k)} = \mathbf{B}_k^{(\ell)} = \begin{bmatrix} 1 & 0 \\ s_\ell(k) & 1 \end{bmatrix} \tag{18}$$

and $\mathbf{B}_k^{(\ell)}$ are unimodular matrices; sampling by these matrices only rearranges the coefficients in the DFB subbands, which can improve its visual effects.

Finally, these matrices are for the first half channels with $0 \le k < 2^{\ell-1}$; the ones for the second half channels are obtained by transposing these matrices. Through appending a downsampling with $\mathbf{B}_k^{(\ell)}$ at the end of the analysis stage of the channel k in the DFB, it becomes equivalent to filtering using $\mathbf{H}_k^{(\ell)}(z)$ followed by downsampling in $\mathbf{S}_k^{(\ell)} = \mathbf{M}_k^{(\ell)}\mathbf{B}_k^{(\ell)}$ where

$$\mathbf{S}_k^{(\ell)} = \begin{cases} \operatorname{diag}(2^{\ell-1}, 2), & 0 \le k < 2^{\ell-1}, \\ \operatorname{diag}(2, 2^{\ell-1}), & 2^{\ell-1} \le k < 2^\ell. \end{cases} \tag{19}$$

Here, $\mathbf{S}_k^{(\ell)}$ is diagonal matrices and sampling by these matrices only rearranges the coefficients in the DFB subbands, which enhances its visualization.

3. Contourlet Filter Design

3.1. Chebyshev Best Uniform Approximation. In order to find the Chebyshev best uniform approximation, there are some theorems, which show conditions for the function $f(x)$ and the approximation expressed as [27]

$$F(A, x) = F(a_0, a_1, \ldots, a_m; x) \tag{20}$$

for which the Chebyshev best uniform approximation can be carried out completely, and $A = \{a_0, a_1, \ldots, a_m\}$, m denote an order Chebyshev approximation. We will provide several theorem to create the condition of existence of the Chebyshev best uniform approximation. We first to define a set of functions as follows. The function $f(x)$ belongs to $\Phi(x, F, w)$ if the following equations are true:

$$\rho(t_0) = -\rho(t_1) = \cdots = (-1)^{m+1}\rho(t_{m+1}), \tag{21}$$

where

$$\rho(x) = \frac{f(x) - F(A, x)}{w(x)}, \qquad a \le t_0 < t_1 < \cdots < t_{m+1} \le b \tag{22}$$

have the unique solution on any subset $T = \{t_i\}_{i=0}^{m+1}$ of the set of points $X \in [a, b]$ and expression $F(A, x)$.

Theorem 1. *Let the approximation expression $F(A, x)$ be continuous for the parameters A, for x if $x \in [a, b]$; $F(A, x) \in \Phi([a, b], F, w)$ and the weight function $w(x) > 0$ is continuous for $x \in [a, b]$. Let $f(x) \in \Phi(X, F, w)$, where*

$$X = \{x_i\}_{i=1}^N, \quad N \ge m + 2, \ X \in [a, b]. \tag{23}$$

Then the following statements are true.

(i) Best Chebyshev weight approximation to the function $f(x)$ on the set X with the help of the expression $F(A, x)$, which satisfies (21), exists and is unique.

(ii) This approximation is completely determined using (21) as follows

$$|\rho(t_0)| = \max|\rho(x)|. \tag{24}$$

(iii) If the initial approximation $T_0 = \{t_i^{(0)}\}_{i=0}^{m+1} = (t_i^{(0)} < t_{i+1}^{(0)})$ for Chebyshev alternate points are chosen in such a way, that the error of approximation in the point $t_0^{(0)}$ is not equal to zero, that is, $\rho(t_0^{(0)}) \ne 0$, then the single point exchange Parks-McClellan algorithm will converge in the final number of steps.

This is a very powerful theorem allows one to minimize the Chebyshev error by directly constructing an equal ripple approximation with the proper number of ripples. The maximal ripple (MR) algorithm formulated the filter design problem by requiring as many ripples as possible. It also imposed an alternating error via an interpolation condition. Instead of directly minimizing the worst-case error, the MR algorithm solved a set of equations that the alternating solution had to satisfy [28, 29]:

$$H_d(\omega_i) + (-1)^i |E(\omega_i)| = \sum_{k=0}^{M} a_k \cos(k\omega_i), \tag{25}$$

where $H_d(\omega_i)$ and $|E(\omega_i)|$ were the desired frequency response of the filter and the desired Chebyshev error, respectively. The term $(-1)^i$ forced the error to alternate on the set of frequencies $\{\omega_i\}$. This set $\{\omega_i\}$ included both ends of the frequency axis, $\omega = 0$ and $\omega = \pi$. Equation (25) contains $M + 1$ undetermined coefficients $\{a_k\}$. The coefficients $\{a_k\}$ can be determined by solving a set of linear equations. Then the issue is how to choose the frequencies $\{\omega_i\}$. With the weight coefficients $\{a_k\}$, the error $E(\omega)$ in the whole frequency domain can completely be viewed as the difference between the desired function $H_d(\omega)$ and its approximation as follows:

$$E(\omega) = H_d(\omega) - \sum_{k=0}^{M} a_k \cos(k\omega). \tag{26}$$

In order to maintain this form, the filter length is $L = 2M + 1$ which must be odd numbers. If there are points where $|E(\omega)| > \varepsilon$, then the frequencies $\{\omega_i\}$ must be corrected. The MR algorithm was to create new set of frequencies using the locations where $E(\omega)$ reached its local maxima, and then iterate this step until $|E(\omega)| \le \varepsilon$. In addition, it is easy to see that a desired function such as

$$H_d(\omega) = \begin{cases} 1, & 0 \le \omega \le \omega_p, \\ 0, & \omega_s \le \omega \le \pi \end{cases} \tag{27}$$

is a continuous function on the closed set $\Omega = [0, \omega_p] \cup [\omega_s, \pi]$, where ω_p and ω_s are the passband and stopband frequencies, respectively. For a continuous function $H_d(\omega)$, the theory of Chebyshev best uniform approximation gaves a necessary and sufficient conditions for designing an optimal filter. Moreover, the alternation theorem of Chebyshev best uniform approximation indicate that the error function $E(\omega)$ in (26) can obtain a maximum absolute value at least $M + 2$ times. Finally, if the frequencies at which the error reaches its maximum absolute value are ordered

$$\omega_1 < \omega_2 < \cdots < \omega_{M+2}, \tag{28}$$

then the maximum error alternates and meaning that

$$|E(\omega_{i+1})| = -|E(\omega_i)| \quad \text{for } i = 1, 2, \ldots, M + 1. \tag{29}$$

Assuming an equiripple type of design, and the ω_p and ω_s are written as

$$\omega_p + \omega_s = \pi, \tag{30}$$

and the ripples are as follows:

$$\delta_1 \approx 10\delta_2. \tag{31}$$

In this case, we can design an equiripple half-band filters using the Parks-McClellan algorithm. The implementation procedure of the Parks-McClellan algorithm is as follows:

(i) Initialization: choose an extremal set of frequencies $\{\omega_i^{(0)}\}$.

(ii) Finite set approximation: calculate the Chebyshev best uniform approximation on the present extremal set giving a value $\delta^{(m)}$ for the min-max error on the present extremal set.

(iii) Interpolation: calculate the error function $E(\omega)$ over the entire set of frequencies Ω using step (ii).

(iv) Lock for local maxima of $|E^{(m)}(\omega)|$ on the set Ω.

(v) If max $\omega \in \Omega$, $|E^{(m)}(\omega)| > \delta^{(m)}$, then update the extremal set to $\{\omega_i^{(m+1)}\}$ by picking new frequencies, where $|E^{(m)}(\omega)|$ has its local maxima. Make sure that the error alternates on the ordered set of frequencies described in term (iv) and (v). Return to the step (ii) and iterate.

(vi) If max $\omega \in \Omega$, $|E^{(m)}(\omega)| \le \delta^{(m)}$, then the algorithm is complete. Use the set $\{\omega_i^{(m)}\}$ and the interpolation formula to compute an inverse discrete Fourier transform to obtain the filter coefficients.

Therefore, we can use the Chebyshev best uniform approximation to the design a lowpass filter as DFB for the contourlet transform. In order to ensure a linear phase filter $H_g(e^{j\omega})$, here we have

$$H\left(e^{j\omega}\right) = e^{-j(n-1)\omega/2} H_g\left(e^{j\omega}\right), \tag{32}$$

$$H_g\left(e^{j\omega}\right) = \sum_{n=1}^{M} a(n) \cos n\omega, \quad M = \frac{N}{2}, \tag{33}$$

where

$$a(n) = 2h\left(\frac{N}{2} - n\right), \quad n = 1, 2, \ldots, \frac{N}{2}. \tag{34}$$

Let $N = 12$; we can obtain an optimal 6-order contourlet filter based on Chebyshev best uniform approximation that, all its coefficients of the filter are determined using the Parks-McClellan algorithm as follows:

$$\begin{aligned} H(z) &= h(1)\left(z + z^{-1}\right) + h(2)\left(z^2 + z^{-2}\right) + h(3)\left(z^3 + z^{-3}\right) \\ &\quad + h(4)\left(z^4 + z^{-4}\right) + h(5)\left(z^5 + z^{-5}\right) + h(6)\left(z^6 + z^{-6}\right), \\ h(1) &= 0.6195, \quad h(2) = -0.1623, \quad h(3) = 0.0528, \\ h(4) &= -0.0012, \quad h(5) = -0.0214, \quad h(6) = 0.1102, \end{aligned} \tag{35}$$

where passband ω_p is 0.4π, stopband ω_s is 0.6π, a peak value of passband wave δ_1 is 0.191929, and peak value of stopband wave δ_2 is 0.019193. This optimal filter is used as a DFB in the Contourlet transform.

3.2. New 9/7 Filter Banks Design. According to [30, 31], we only need to design both the lowpass filters $H_0(z)$ and $G_0(z)$ of the 9/7 filter banks on analysis and synthesis stage respectively, also all the coefficients of the 9/7 filter banks family and their lifting parameters with respect to a one control variable ξ are shown in (36) and (37).

According to the corresponding coefficients between (36) and (37), when $\xi = 1.34$, all the coefficients of lowpass filter and highpass filter in the analysis and synthesis stages respectively, and all the lifting parameters can completely be determined, and they are listed in Table 1:

$$
\begin{aligned}
h(0) &= -\frac{8\xi^3 - 18\xi^2 + 7\xi - 20}{16\xi},\\
h(1) &= \frac{4\xi^3 - 11\xi^2 + 15\xi - 4}{8\xi},\\
h(2) &= \frac{\xi - 2}{4\xi},\\
h(3) &= \frac{(4\xi^2 - 7\xi + 4)(\xi - 1)}{8\xi},\\
h(4) &= \frac{(4\xi^2 - 7\xi + 4)(2\xi - 1)}{32\xi},\\
g(0) &= \frac{\xi + 1}{4},\\
g(1) &= \frac{2\xi + 7}{32},\\
g(2) &= -\frac{\xi - 1}{8},\\
g(3) &= -\frac{2\xi - 1}{32},\\
\alpha_1 &= \frac{1 - 2\xi}{4(\xi - 1)},\\
\alpha_2 &= -(\xi - 1)^2,\\
\alpha_3 &= \frac{1}{4\xi(\xi - 1)},\\
\alpha_4 &= \xi^3 - \frac{7}{4}\xi^2 + \xi,\\
K &= \frac{2}{\xi}.
\end{aligned}
\tag{36}\tag{37}
$$

4. Contourlet Domain HMT Models

4.1. Model Definition. We know that compositionality in a generative stochastic model can be achieved using probabilistic independence. According to [32, 33], the structure of hidden Markov tree models can be graphically described through the belief networks as shown in Figure 6, where black and white notes represent observation and hidden class variables, respectively.

Also, Y denote a labeled m-ary tree, and each node v is labeled by a K-tuple of random variables, and is denoted by $Y(v)$. For each tree Y, we can write $P(Y) = P(Y(r), Y_1, Y_2, \ldots, Y_m)$, where $Y(r)$ is the label at the root node r and Y_i are random subtrees. In addition, we see that the first-order Markov tree property is satisfied for Y if the following formula is true:

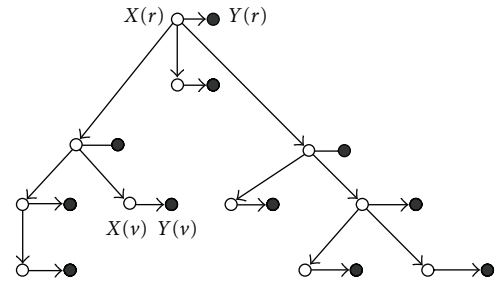

Figure 6: Structure of hidden Markov tree models.

$$P\left(Y_i \mid Y_j, Y(r)\right) = P(Y_i \mid Y(r)), \quad \forall i, j = 1, 2, \ldots, m. \tag{38}$$

From this property, the following expression can be proved by the induction:

$$P(Y) = P(Y(i)) \prod_{v \in V \setminus \{r\}} P\left(Y(v) \mid Y\left(pa[v]\right)\right), \tag{39}$$

where $pa[v]$ denotes the parent of vertex v and V denotes the set of vertices of Y. However, the model formulated by (39) has two disadvantages. First, the conditional independence assumption as shown in (38) is unrealistic and does not allow the model to capture correlations between any two nonadjacent nodes. Second, the parameterization of $P(Y(v) \mid Y(pa[v]))$ might be problematic since the number of parameters grows exponentially with the number of attributes in each label. Here, we let $\chi = \{x_1, x_2, \ldots, x_n\}$ be a finite set of states. And, we assume that each tree $\mathbf{Y}$ is generated by an underlying hidden tree $\mathbf{X}$, a data structure defined as follows: the skeleton of $\mathbf{X}$ is identical to the skeleton of $\mathbf{Y}$. Nodes of $\mathbf{X}$ are labeled by hidden state variables $X(v)$, taking realizations on χ. In this way, $P(\mathbf{Y}) = \sum_{\mathbf{X}} P(\mathbf{X})$, where the sum over $\mathbf{X}$ indicates the marginalization over all the hidden trees. The first-order tree-Markov property in the case of hidden tree models holds if the two following conditions are exist.

(i) The first-order tree-Markov property must hold for the hidden tree **X.**

(ii) For any possible v, the observation $Y(v)$ is independent of the rest given $X(v)$.

These conditions imply the following global factorization formula:

$$
\begin{aligned}
P(\mathbf{Y}, \mathbf{X}) &= P(X(r))P(Y(r) \mid X(r))\\
&\quad \times \prod_{v \in V \setminus \{r\}} P(Y(v) \mid X(v))P\left(X(v) \mid X\left(pa[v]\right)\right).
\end{aligned}
\tag{40}
$$

The corresponding stochastic model is a hidden Markov tree (HMT) model.

Table 1

(a) All the coefficients of new 9/7 filter banks

Number	Analysis filter		Synthesis filter	
k	lowpass	highpass	lowpass	highpass
0	117/200	370187/335000	370187/335000	117/200
±1	−121/400	−373301/670000	373301/6700000	121/400
±2	−17/400	−33/268	−33/268	−17/400
±3	21/400	−38301/670000	38301/670000	−21/400
±4		757/10720	757/10720	

(b) All the lifting parameters of new 9/7 filter banks

Parameters	Values
α_1	−21/17
α_2	−289/2500
α_3	625/1139
α_4	150951/250000
K	100/67

4.2. Parameterization. According to (40), we know that parameters for the HMT model are $P(X(r))$, a prior on the root hidden state, $P(Y(v) \mid X(v))$, the emission parameters, and $P(X(v) \mid X(pa[v]))$, the transition parameters. These parameters vary with the node, and will generate a large total number of parameters that might result in overfitting issue. In addition, we see that a HMT model is fully stationary if it is both transition and emission stationary. In this case, the total number of parameters is $n(1+n+K)$ being K the number of parameters in each emission model $P(Y \mid X = x)$. Moreover, we also know that the above model is locally stationary if it is emission stationary and

$$P(X(v) \mid X(pa[a])) = P(X(\omega) \mid X(pa[\omega])), \tag{41}$$

where v and ω are both the ith children of their parent in the tree. This assumption will yield $n(1 + nm + K)$ parameters. Finally, the model mentioned above is level stationary if the following formulae are true:

$$\begin{aligned} P(X(v) \mid X(pa[v])) &= P(X(\omega) \mid X(pa[\omega])), \\ P(Y(v) \mid X(v)) &= P(Y(\omega) \mid X(\omega)), \end{aligned} \tag{42}$$

where v and ω belong to the same level of the tree.

4.3. Inference and Learning. Inference consists of computing all the conditional probabilities of hidden states, given the evidence entered into the observation nodes. Since the network as shown in Figure 6 is singly connected, the inference problem can be solved either by π-λ propagation or by the junction tree algorithm [34]. Given such structure of the HMT model in Figure 6, no moralization is required and cliques forming the junction tree are of two kinds: one containing $X(v)$ and $X(pa[v])$, the other one containing $Y(v)$ and $X(v)$. In both cases, only two variables are contained in a clique. It should be remarked that $P(Y)$ is simply obtained as the normalization factor in any clique after propagation in the junction tree. Inference in HMT model is very efficient and runs in time proportional to the number of nodes in $\mathbf{Y}$ and to the number of states in χ. Each model λ_i is trained using examples belonging to class c_i. Learning is formulated in the maximum-likelihood framework and the presence of hidden variables requires an iterative algorithm for solving the optimization problem. In the implementation above, the Expectation-Maximization (EM) algorithm is chosen [35].

5. Results and Discussion

We partition the finest and second finest scales into eight directional subbands, and the two next coarser scales into four directional subbands, and obtain a frequency partition. In order to verify the effectiveness of the two novel filters for image denoising in the contourlet HMT model, we choose a texture images that vary from simple edge dominant images to highly textured images such as Barbara, a grayscale image of resolution 512×512 pixels and 8 bits per pixel.

The experimental platform is in a CPU3.0 GHz, memory 2.0 GB, and Windows XP. And, a control variable ξ of the 9/7 filter banks family is selected as $[0, 4]$; the interval of a control variable ξ is 0.1. According to denoising method of [12], we carried out the image denoising experiments to test image Barbara, the results are shown in Figure 7.

In addition, we choose a control variable ξ in the interval of 0.001 to implement the image denoising and the performances of tested results are shown in Figure 8. Moreover, we chooses five datasets, formed by the values on the upper layers in Figure 8, to complete the data fitting using a fourth-order polynomial for each dataset; the resulting curves are shown in Figure 9. From this figure we can see that the five fitting curves almost focus on a single point at 1.34; we take 1.34 as the optimal point: $\xi_{\text{opt}} = 1.34$. Given ξ_{opt} all the coefficients and the lifting parameters of the optimal 9/7 filter banks are rational numbers and are determined completely through (36) and (37), the results are listed Table 1. Moreover, if the above two optimal filter banks are

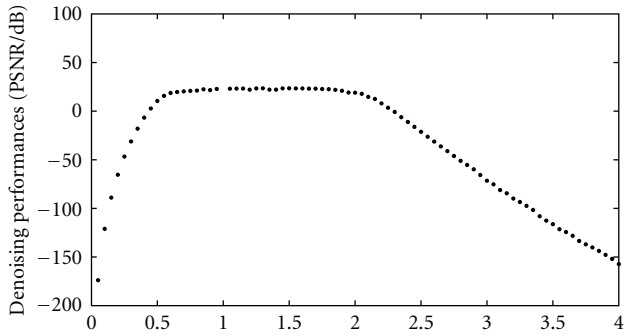

Figure 7: The results of image denoising.

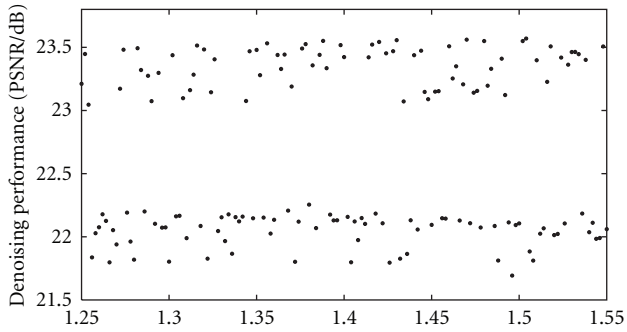

Figure 8: Denoising result within a narrow range.

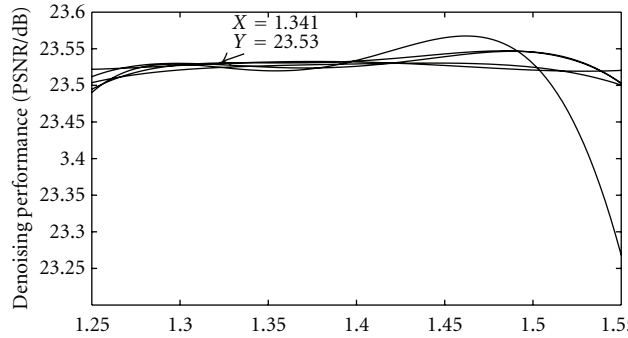

Figure 9: Data fitting result about optimal samples.

Table 2: Denoising effects comparison for different images on various noise levels (PSNR in dB).

Image	Noise level σ	Po and Do's method	Our method
Lena	30	28.18	28.42
	40	27.00	27.14
	50	26.04	26.32
Barbara	30	25.27	25.20
	40	24.79	24.45
	50	23.74	23.58
Zelda	30	30.00	29.98
	40	28.29	28.46
	50	27.07	27.40

used in the contourlet HMT model and on the experimental platform presented by Po and Do [12], the image denoising performance in terms of the PSNR is maximum and equals 23.53 dB.

In [12], Po and Do used the CDF 9/7 filter on the LP decomposition stage and pkva 12 filter on the DFB decomposition stage in the contourlet HMT model for image denoising. This paper differs from [12] in the use of both new 9/7 filter with rational coefficients and their lifting implementation, and new pkva 12 filter above on the LP and DFB decomposition stage, respectively. Since the new 9/7 filter banks are all the rational coefficients, so that the computational complexity can greatly be reduced, VLSI hardware implementation becomes easier and speeds up by 50% than the CDF 9/7 filter banks with irrational coefficients. As an objective comparison between the two methods, the image denoising effects using contourlet domain HMT models for different images on various noise levels are shown in Table 2.

From Table 2 we see that the our method improved image denoising with 0.33 and 0.28 dB compared to [12] for images Zelda and Lena, respectively; it is only 0.16 dB less compared with the result of [12] for the Barbara image denoising while the noise level σ equals 50. Because the Lena is a smooth image with many of the low-frequency areas than Barbara which is a texture image with many of the high-frequency details, so that the proposed approach works better for the image denoising compared to [12]. Also, since the low-frequency areas of the Zelda image are fewer than the Lena image, thus the denoisng performances of the Zelda image are slightly lower quality than the Lena image.

Moreover, we present also the subjective comparison using the new 9/7 filter banks with rational coefficients mentioned above on the LP decomposition stage and the new pkva 12 filter on the DFB decomposition stage in the contourlet domain HMT model; the results are shown in Figure 10. In Figure 10(b), Gaussian noise with $\sigma = 50$ is added to the original image. Comparing Figures 10(c) and 10(d) we can see that the visual quality using the image denoising approach of this paper is as good as the result of [12].

6. Conclusions

The design approach for the contourlet filter banks based on the Chebyshev best uniform approximation method is effective, and both the optimal 9/7 filter banks with rational coefficients and the new pkva 12 filter for implementing the Zelda image denoising in the contourlet HMT models are improved by 0.33 dB. Also, the contourlet HMT model based on the above two filter banks is improved for the other image denoising applications. Particularly, since the optimal 9/7 filter banks with rational coefficients have two advantages of the low computational complexity and easy hardware implementation, so that the image denoising approach presented in this paper can widely be applied to the digital camera and multimedia device.

(a) (b) (c) (d)

Figure 10: Subjective comparison for denoising performance, (a) original image, (b) noise image, (c) Po and Do's result, and (d) our result.

Acknowledgments

This work was supported by the Chinese National Natural Science Foundation under Grants 60635050 and 2010CA322001, and project 973 of National Key Basic Research of China under Grant 2007CB311005.

References

[1] M. Vetterli and J. Kovacevic, *Wavelets and Subband Coding*, Prentice-Hall, Englewood Cliffs, NJ, USA, 1995.

[2] S. Mallat, *A Wavelet Tour of Signal Processing*, Academic Press, New York, NY, USA, 2nd edition, 1999.

[3] S. G. Mallat, "A theory for multiresolution signal decomposition: the wavelet representation," *IEEE Transactions on Pattern Analysis and Machine Intelligence*, vol. 11, no. 7, pp. 674–693, 1989.

[4] M. Antonini, M. Barlaud, P. Mathieu, and I. Daubechies, "Image coding using wavelet transform," *IEEE Transactions of Image Processing*, vol. 1, no. 2, pp. 205–220, 1992.

[5] E. J. Candès and D. L. Donoho, "Curvelets: a surprisingly effective nonadaptive representation for objects with edges," in *Curve and Surface Fitting*, Vanderbilt University Press, Nashville, Tenn, USA, 2000.

[6] F. G. Meyer and R. R. Coifman, "Brushlets: a tool for directional image analysis and image compression," *Applied and Computational Harmonic Analysis*, vol. 4, no. 2, pp. 147–187, 1997.

[7] E. P. Simoncelli, W. T. Freeman, E. H. Adelson, and D. J. Heeger, "Shiftable multiscale transforms," *IEEE Transactions on Information Theory*, vol. 38, no. 2, pp. 587–607, 1992.

[8] N. Kingsbury, "Complex wavelets for shift invariant analysis and filtering of signals," *Applied and Computational Harmonic Analysis*, vol. 10, no. 3, pp. 234–253, 2001.

[9] M. N. Do and M. Vetterli, "Contourlets," in *Beyond Wavelets*, G. V. Welland, Ed., pp. 83–105, Academic Press, New York, NY, USA, 2003.

[10] M. N. Do and M. Vetterli, "The contourlet transform: an efficient directional multiresolution image representation," *IEEE Transactions on Image Processing*, vol. 14, no. 12, pp. 2091–2106, 2005.

[11] M. N. Do, *Directional multiresolution image representations*, Ph.D. dissertation, School of Computer and Communication Sciences at EPFL-Swiss Federal Institute of Technology, Lausanne, Switzerland, December 2001.

[12] D. D. Y. Po and M. N. Do, "Directional multiscale modeling of images using the contourlet transform," *IEEE Transactions on Image Processing*, vol. 15, no. 6, pp. 1610–1620, 2006.

[13] R. H. Bamberger and M. J. T. Smith, "A filter bank for the directional decomposition of images: theory and design," *IEEE Transactions on Signal Processing*, vol. 40, no. 4, pp. 882–893, 1992.

[14] P.J. Burt and E. H. Adelson, "The Lapacian pyramid as a compact image code ," *IEEE Transactions on Communications*, vol. 31, no. 4, pp. 532–540, 1983.

[15] G. Beylkin, "Discrete Radon transform," *IEEE Transactions on Acoustics, Speech, and Signal Processing*, vol. 35, no. 2, pp. 162–172, 1987.

[16] E. J. Candès, *Ridgelets: Theory and Applications*, Ph.D. thesis, Department of Statistics, Stanford University, Palo Alto, Calif, USA, 1998.

[17] A. Cohen, I. Daubechies, and J.-C. Feauveau, "Biorthogonal bases of compactly supported wavelets," *Communications on Pure and Applied Mathematics*, vol. 45, pp. 485–560, 1992.

[18] I. Daubechies, "Orthonormal bases of compactly supported wavelets," *Communications on Pure and Applied Mathematics*, vol. 41, pp. 909–996, 1988.

[19] I. Daubechies, "The wavelet transform, time-frequency localization and signal analysis," *IEEE Transactions on Information Theory*, vol. 36, no. 5, pp. 961–1005, 1990.

[20] ISO/IEC15444-1, ITU-TRec.T.800, "JPEG2000 image coding system," part 1 (core).

[21] ISO/IEC15444-2, ITU-T Rec. T.800, "JPEG2000 image coding system," part 2 (extensions).

[22] S.-M. Phoong, C. W. Kim, P. P. Vaidyanathan, and R. Ansari, "A new class of two-channel biorthogonal filter banks and wavelet bases," *IEEE Transactions on Signal Processing*, vol. 43, no. 3, pp. 649–665, 1995.

[23] M. Vetterli and C. Herley, "Wavelets and filter banks: theory and design," *IEEE Transactions on Signal Processing*, vol. 40, no. 9, pp. 2207–2232, 1992.

[24] Z. Cvetković and M. Vetterli, "Oversampled filter banks," *IEEE Transactions on Signal Processing*, vol. 46, no. 5, pp. 1245–1255, 1998.

[25] B. A. Olshausen and D. J. Field, "Sparse coding with an overcomplete basis set: a strategy employed by V1?" *Vision Research*, vol. 37, no. 23, pp. 3311–3325, 1997.

[26] J. Kovačević and M. Vetterli, "Nonseparable multidimensional perfect reconstruction filter banks and wavelet bases for R^n," *IEEE Transactions on Information Theory*, vol. 38, no. 2, pp. 533–555, 1992.

[27] B. Popov, "Nonlinear best chebyshev approximations and splines," in *Proceedings of the IEEE Conference on Mathematical Methods in Electromagnetic Theory (MMET '96)*, pp. 128–131, 1996.

[28] L. J. Karam and J. H. McClellan, "Complex chebyshev approximation for FIR filter design," *IEEE Transactions on Circuits and Systems II*, vol. 42, no. 3, pp. 207–216, 1995.

[29] J. H. McClellan and T. W. Parks, "A personal history of the Parks-McClellan algorithm," *IEEE Signal Processing Magazine*, vol. 22, no. 2, pp. 82–86, 2005.

[30] G. Yang and N. Zheng, "A optimization algorithm for biorthogonal wavelet filter banks design," *International Journal of Wavelets, Multiresolution and Information Processing*, vol. 6, no. 1, pp. 51–63, 2008.

[31] G. Yang, N. Zheng, and S. Guo, "Optimal wavelet filter design for remote sensing image compression," *Journal of Electronics*, vol. 24, no. 2, pp. 276–284, 2007.

[32] M. S. Crouse, R. D. Nowak, and R. G. Baraniuk, "Wavelet-based statistical signal processing using hidden Markov models," *IEEE Transactions on Signal Processing*, vol. 46, no. 4, pp. 886–902, 1998.

[33] M. Diligenti, P. Frasconi, and M. Gori, "Hidden tree Markov models for document image classification," *IEEE Transactions on Pattern Analysis and Machine Intelligence*, vol. 25, no. 4, pp. 519–523, 2003.

[34] F. V. Jensen, S. L. Lauritzen, and K. G. Olosen, "Bayesian updating in recursive graphical models by local computations," *Computational Statistical Quarterly*, vol. 4, pp. 269–282, 1990.

[35] A. Zia, T. Kirubarajan, J. P. Reilly, D. Yee, K. Punithakumar, and S. Shirani, "An EM algorithm for nonlinear state estimation with model uncertainties," *IEEE Transactions on Signal Processing*, vol. 56, no. 3, pp. 921–936, 2008.